Geophysical Investigation of Noctis Volcano on (equatorial) Mars using MOLA, MARSIS, and Numerical Plume Modelling.

Faris Beg[1] and Adrien Broquet[2]

[1]Affiliation not available
[2]German Aerospace Center

November 03, 2025

Abstract

Most Martian volcanoes have been fed by stationary mantle plumes, leading to the buildup of large shield edifices. A recent investigation on a poorly mapped region, located between equatorial Noctis Labyrinthus and Valles Marineris, revealed a heavily fractured structure, initially interpreted to be an ancient shield volcano called Noctis Mons. This work uses orbital data and geophysical models to unravel the volcano-tectonic formation history of Noctis Mons. Using topographic data, the pre-fracture structure of Noctis Mons is revealed and found to resemble typical small volcanic Martian shields, with a height of ~8694 m. Ancient plume-induced uplift is also observed and compared to an analytical elastic flexure model. Our results indicate Noctis was fed by a ~470 km wide and ~70 km thick mantle plume head. Analyses of radar data suggest a large part of Noctis is made of highly porous (~51%) basalt, suggesting intense explosive activity and potential phreatomagmatism with magma interacting with Valles Marineris water in the Hesperian.

Hosted file

`possible cover picture .png` available at https://authorea.com/users/993013/articles/1355127-geophysical-investigation-of-noctis-volcano-on-equatorial-mars-using-mola-marsis-and-numerical-plume-modelling

Posted on 3 Nov 2025 — CC-BY-NC-ND 4 — https://doi.org/10.22541/essoar.176218868.89744519/v1 — This is a preprint and has not been peer-reviewed. Data may be preliminary.

Nantes
Université

Table of Contents

Geophysical Investigation of Noctis Mons

Faris Beg
Supervisor: Adrien Broquet[1]

October31, 2025

Abstract

Most Martian volcanoes have been fed by stationary mantle plumes, leading to the buildup of large shield edifices. A recent investigation on a poorly mapped region, located between equatorial Noctis Labyrinthus and Valles Marineris, revealed a heavily fractured structure, initially interpreted to be an ancient shield volcano called Noctis Mons. This work uses orbital data and geophysical models to unravel the volcano-tectonic formation history of Noctis Mons. Using topographic data, the pre-fracture structure of Noctis Mons is revealed and found to resemble typical small volcanic Martian shields, with a height of ~8694 m. Ancient plume-induced uplift is also observed and compared to an analytical elastic flexure model. Our results indicate Noctis was fed by a ~470 km wide and ~70 km thick mantle plume head. Analyses of radar data suggest a large part of Noctis is made of highly porous (~51%) basalt, suggesting intense explosive activity and potential phreatomagmatism with magma interacting with Valles Marineris water in the Hesperian.

[1] Department of Planetary Physics, German Aerospace Center (DLR)

Introduction:

Volcanism has shaped Mars from its earliest days, leaving behind some of the largest and most diverse volcanic landscapes in the Solar System. Volcanic history of Mars can be studied in three main stages based on its chronological periods estimated through cratering rate and chronology models (Ivanov, 2001). The three stages are Noachian (4.1-3.7 Ga), Hesperian (3.7-2.9 Ga), and Amazonian (2.9 Ga-present). Little is known about the volcanism and surface conditions during the pre-Noachian (4.5 Ga-4.1 Ga) (H. Carr & W. Head, 2010). During the Noachian, Tharsis appeared, as indicated by primary volcanic deposits like basalts rich in calcium pyroxene, as well as olivine (Poulet, 2005). Typically, cratered Noachian highlands are comprised of basalts, pyroclastic flows, and impact breccias (Squyres, 2007) with many rocks showing signs of aqueous alteration suggesting hydrothermal activity (H. Carr & W. Head, 2010). During Hesperian, volcanism remained widespread and resulted in resurfacing about 30% of the planet (Head, 2002). Hesperian volcanism was characterized by ridged plains and low-shield-like edifices. Extensive dykes, hundreds of kilometers long, likely fed these edifices causing effusive flood basalt volcanism and depositing pyroclastic material (Head, Modification of the dichotomy boundary on Mars by Amazonian mid-latitude regional glaciation, 2006). During the Amazonian, eruptions were largely confined to the outer edges of Tharsis and Elysium, where numerous shield volcanoes dominate. Rheological properties and crater counting statistics indicate volcanic activity in the last tens of millions of years. Similarly, Martian meteorite samples exhibit crystallization ages as young as 150 Ma (McSween, 2002), demonstrating that Mars remains sporadically active, albeit at very low rates, falling from about 1 km^3/yr in Hesperian to approximately 0.1 km^3/yr in the Amazonian (H. Carr & W. Head, 2010)

Similar to Earth, Mars’s volcanoes are primarily made of basaltic material (McSween, 2002), erupting low-viscosity lavas that flow over hundreds of kilometers, but the lower gravity and thin atmosphere allows both longer flows and more explosive, ash-rich Plinian eruptions (Carr, 2007). Rheological properties of some lava flows in Tharsis and Elysium region (Hauber, 2011) reveal the basaltic terrains are only tens of millions of years old. Similarly, Crater statistics and Martian meteorite samples exhibit crystallization ages as young as 150 Ma (McSween, 2002), demonstrating that Mars remains sporadically active, albeit at very low rates averaged over hundreds of millions of years. The mechanism governing volcanism on Mars is similar to how Earth’s magmas mobilize, with the partial melting of mantle or crustal materials, followed by ascent through dykes and sills, with potential storage in shallow crustal magma chambers (Wilson & Head III, 1994) (McSween, 2002).

In this study, we investigate one region located south-east of the Tharsis Montes (Figure 1), which has been provisionally designated as an ancient shield volcano, called Noctis Mons (Lee & Shubham, 2024). Noctis Mons is positioned at 7.4°S 265.4°E, in between Noctis Labyrinthus and Valles Marineris, in a region characterized by a complex intersection of extensional rift valleys or canyons presenting a tectonically fractured topography. Due to the complexity of the Mons’ regional topography, it is difficult to propose a definitive chronological history of volcanic edifice formation and collapse. Nonetheless, certain features show a clearer picture of events that may have led to the present topography. For example, the stepped morphology (reported by Lee et al, 2024) of the volcanic remnant could be interpreted as a continuation of the Valles Marineris rift system, however, the pronounced concentric radial symmetry of its summit, flanks, and surrounding mesas indicates instead a sequential gravitational collapse of summit sectors at different intervals. Nevertheless, the Noctis Mons feature remains largely under-studied and poorly mapped for most part. For example, (Tanaka, 2014), in their global geological map of Mars, partly designate this region as the Noachian Highland Undivided (HNu) unit, which corresponds to highland terrain formed during the early Noachian. While the work of Lee et al. (2024) provided geomorphological and composition supporting a volcanic origin for Noctis, such hypothesis has not been tested against geophysical data. In this work, we use geophysical methods and modelling to test whether Noctis Mons could indeed represent the remnant of an ancient shield volcano. In particular, we determine if a classical plume-induced volcanic shield sequence can explain the geomorphology of present-day Noctis Mons.

Volcano-tectonic context

The tectonic features observed in the Noctis region are predominantly graben-style extensional faults, mapped over plains of late Noachian and late Hesperian ages (Knapmeyer, 2006). Stress created by loading of Tharsis Montes, most likely created the graben style opening of the Valles Marineris (Andrews-Hanna, 2012) (H. Carr & W. Head, 2010). Because Tharsis appears to have largely formed by the end of the Noachian, it is likely that the canyons of Valles Marineris started to form in the late Noachian and continuing to the early Hesperian (Webb & Head, III, 2002).

Another tectonic influence over Noctis Mons comes from the vast sloping Thaumasia Plateau in the south (Figure 1). A study (Montgomery, 2006) proposed a tectonic deformation aided by salt tectonics on the plateau like a “mega-slide” originating in North-West, North-East and continuing towards South-Eastern Solis Planum, forming wrinkle ridges towards the end of the slide, where compression begins (Figure 1). The Thaumasia slide would have caused or reactivated the fractures on the North-East side of the Thaumasia Plateau, i.e., Valles Marineris and Noctis Mons, aligning with the fault distribution pattern that indicate opening of a shield volcano as we annotate with strike-dip symbols in Figure 1. Although volcanics on Mars do not differ much from terrestrial volcanics, absence of plate tectonics on Mars implies that, unlike Earth’s volcanoes which migrate with moving plates, Martian volcanism can lead to enormous volcanic edifices being built over a single hotspot. Following this, the series of three Tharsis volcanoes, namely Arsia Mons, Ascraeus Mons, and Pavonis Mons in a linear northeast–southwest trend (Figure 1), are proposed to have formed by a single, long-lived, mantle plume upwelling feeding successive eruptions over a billion-year span (Harder &

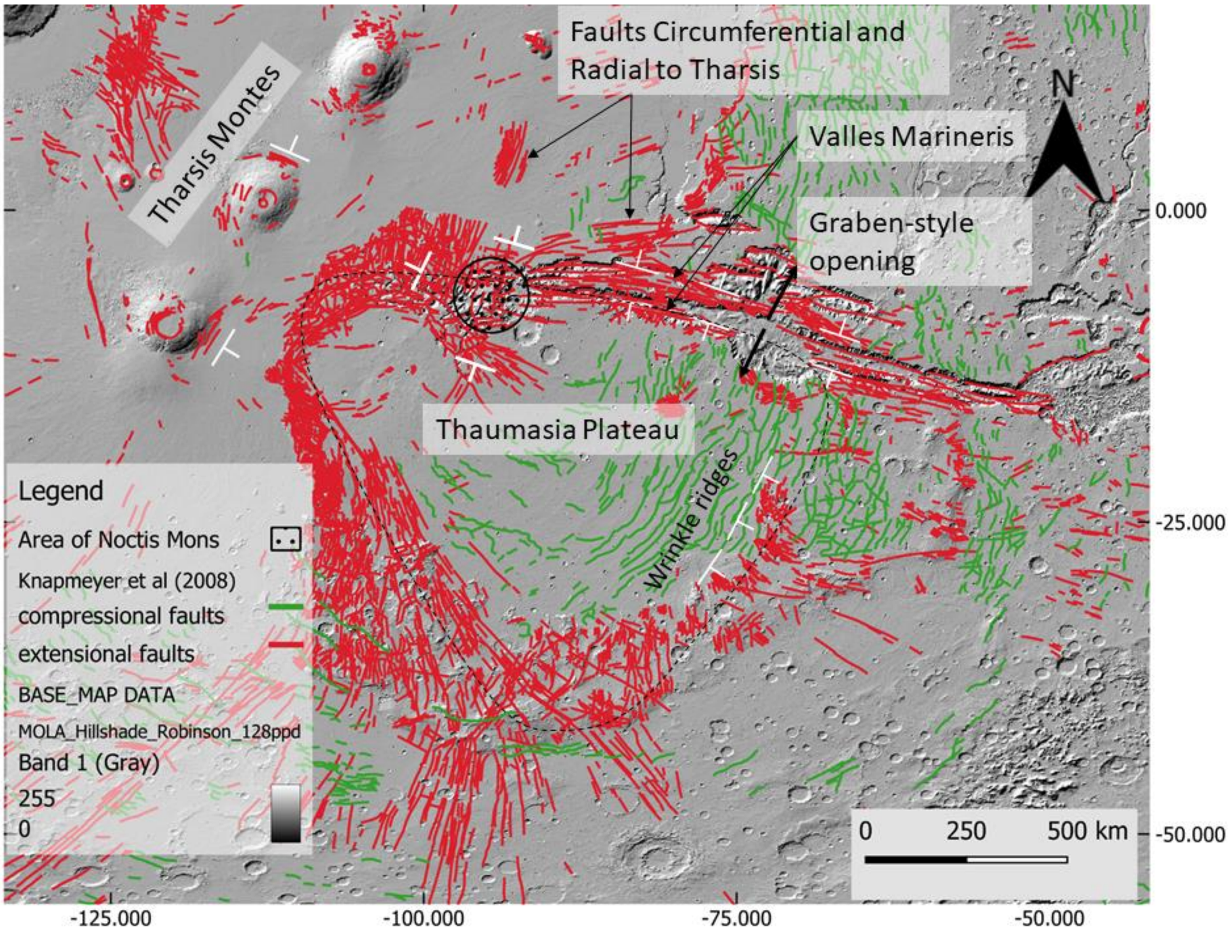

Figure 1: Tectonic landforms in the Thaumasia Plateau over a Mars MOLA Hillshade background. Graben (red) and compressional ridges (green) (Knapmeyer, 2006) distribution indicates orientation radial to Tharsis inducing a graben style opening of Valles marineris and Noctis Mons. Strike-dip T symbols overlaying faults are added for orientation.

Christensen, 1996). A similar single dynamic plume model can also be developed for Noctis Mons as we will discuss in later sections.

Water-Magma Interaction

The permafrost and groundwater were present in the upper crust during Mars' early history (Carr M. , 1987) implying substantial early phreatomagmatism (magma–water interaction). Wilson and Head (2007) revisited magmatic ascent, emplacement, and eruption on Mars and presented a theoretical treatment of phreatomagmatic hydrothermal interaction. In their synthesis, several modes of hydrothermal interactions are presented such as emplacement of Martian magma as intruding thin, sheet-like dikes or sills into the ice-rich substrate delivering heat efficiently through a large surface-to-volume interface. This intrusion can cause rapid melting of surrounding permafrost destabilising the overlying rocks, leading to localized subsidence, collapse structures, or the formation of outflow channels (Wilson & Head, 2007). Similarly, conductive heating from overlying lava flows can vaporize subsurface groundwater or ice substrate explosively, leading to lava fragmentation that produces rootless pyroclastic deposits, or pseudocraters called rootless cones (Thorarinsson, 1953) (Lee et al 2024).

Given the highly eroded nature of Noctis, it is likely that phreatomagmatism played a substantial role in the formation of that edifice. In the following sections, we first develop a schematic model illustrating the sequence of events that lead to collapsed Noctis Mons topography we observe today. Then we describe the various types of orbital datasets used in this study and develop the associated methodology. The results obtained using orbital datasets help us reconstruct the elevation map of Noctis Mons, calculate the volume occupied by the volcanic construct within the region, estimate the uplifted plain, and compare it with a numerically modeled uplift. We develop a hypothesis of a mantle plume generated flexural uplift in an elastic lithosphere. Finally, we will discuss the composition of the pyroclastic material making up the bulk of the Noctis topography and investigate the possibility of subsurface ice deposits proposed in Lee et al (2024).

Data and Methods:

Schematic Chronology

Reconstructing Noctis Mons’s evolution from formation to collapse is challenging. Figure 2 presents a simplified history for Noctis based on our orbital and geophysical–geodynamic analyses, and that can be described as follows. Plume upwelling beneath Noctis Mons likely began with the tectonic opening of Valles Marineris between late Noachian and early Hesperian (Webb & Head, III, 2002) induced by flexural stresses of the Tharsis bulge (Andrews-Hanna, 2012) (H. Carr & W. Head, 2010). Faults circumferential and radial to Tharsis coincide with: a) graben style NW extensional fault pattern on the margins of Valles marineris (Figures 1 and 2b) and b) faults circumferential to sub-circular Noctis Mons region (Figures 1, 2a, and 8) (Knapmeyer, 2006). Considering a flexural response of the elastic lithosphere (Banerdt, Phillips, Sleep, & Saunders, 1982), the plume generated a lithospheric uplift (Figure 2b), inducing the formation of a circumferential pattern of extensional faults (Figure 2b).

Previous studies have recorded evidence for abundant groundwater and surface discharge during this period (late Noachian-Early Hesperian), as flood channels emerged from chaotic terrain in canyon floors of Valles Marineris (Harrison & Grimm, 2008). Following Wilson and Head (2007), conductive heating from surface lava likely vaporised subsurface groundwater resulting in explosive phreatomagmatic activity, creating rootless cones (Lee & Shubham, 2024) and depositing porous pyroclastic ash (Figure 2c). In the final stage, following the phreatomagmatic subsidence and collapse mechanism described above (Wilson & Head, 2007), the subsurface magmatic emplacement interacting with permafrost likely lead to the

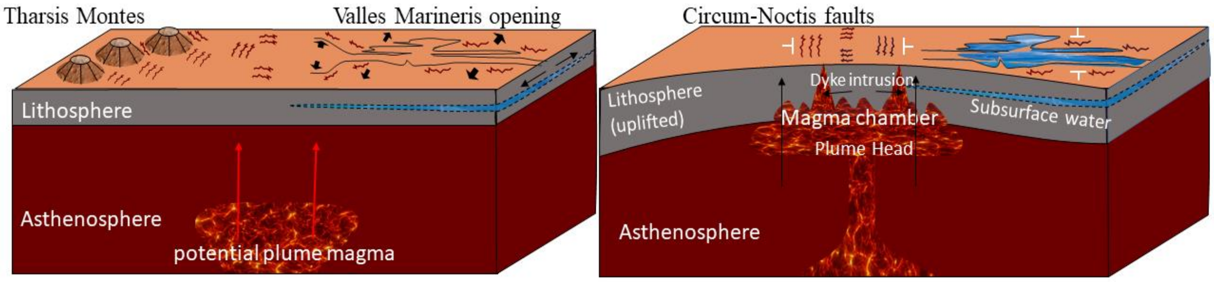

a) Tharsis bulge stresses opened Valles Marineris, facilitating plume ascent (Andrews-Hanna, 2012).

b) Plume impinges Noctis region; flexural uplift in lithosphere; extension accompanied by dyke intrusion

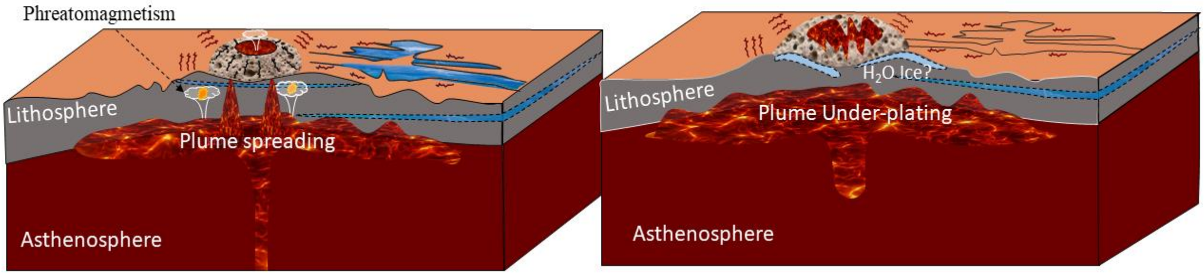

c) Plume spreading; magma-water interaction; basaltic flood lava + porous volcanic pyroclast deposititon

d) Caldera collapse; weathering and fracturing of Noctis topography; plume head under-plating sustains regional uplift

Figure 2: 3D Schematic Diagram of the chronological stages in the life of Noctis Mons

caldera collapse, in combination with gravitational inward collapsing and erosion of the porous pyroclastic ash deposits, resulting in mesas like stepped morphology (Lee & Shubham, 2024).

Spherical Harmonics and MOLA Data

Our forthcoming analyses will rely on elevation data. Mars shape and topography have been globally characterised by the Mars Orbiter Laser Altimeter (MOLA) onboard NASA's Mars Global Surveyor. MOLA mapped Mars pole-to-pole from March 1998 firing 1.064 µm laser pulses through a 0.5 m telescope and detected returns with a fast photodiode/timing system, measuring 160 m-wide spots every 300 m along its ground track (Smith, 2001). It measured round-trip pulse times with 37 cm precision and, after correcting for orbit and pointing, produced elevation profiles accurate to about 1 m vertically and 100 m horizontally.To estimate the pre-fracture and collapse topography of the Noctis Mons, to calculate the volume occupied by pyroclastic deposits in the region, as well as to analyze the uplift of the plain beneath Noctis Mons, we analyze MOLA topography data in the spherical harmonic domain. We perform matrix operations on the digital-elevation-model grids which are retrieved as Mars Orbiter Laser Altimeter (MOLA) topography datasets via *pyshtools* package. Specifically, we load the "MOLA_shape" dataset: a global topography expressed as a spherical-harmonic expansion up to degree and order 5759 (Wieczorek & Meschede, 2018). Fundamentally, spherical harmonic functions can be seen as equivalent to 2D Fourier transforms on a sphere. Spherical harmonics are by construction solutions to Laplace's equation and are particularly useful when analysing topography data on a sphere. The spherical harmonics depends on two main parameters the degree ℓ (controls resolution) and the order m (controls longitudinal variation). Working in the spectral domain (spherical harmonics coefficients) gives us a certain edge in data processing, which was proven useful when interpolating elevation data to reconstruct Noctis Mons. The spherical harmonic coefficients of topography are expanded onto a global grid (Figure 3).

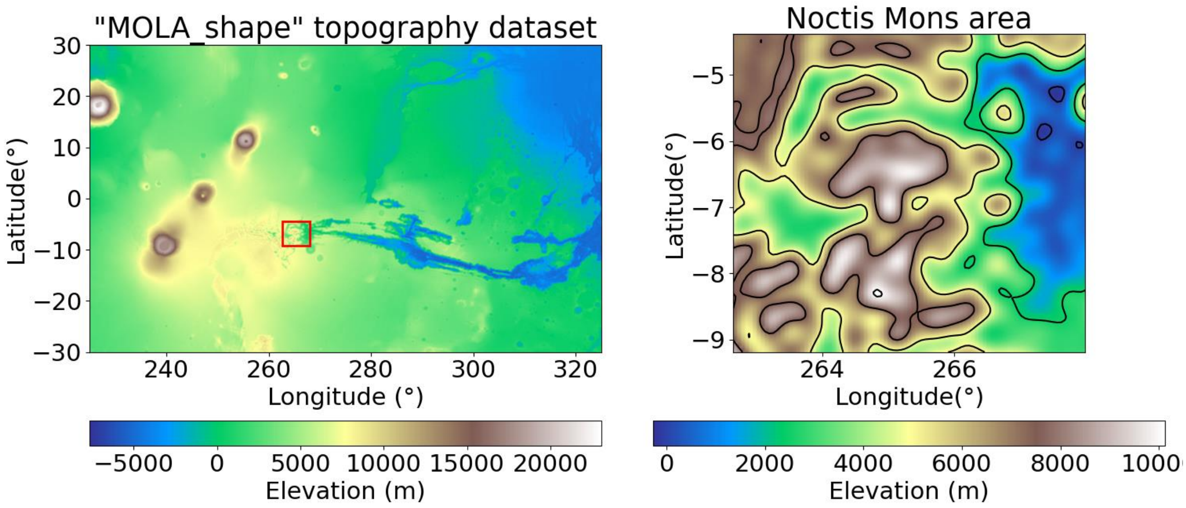

Figure 3: Regional MOLA elevation map (left). Zoomed in elevation contour map of the Noctis Mons area. MOLA topography dataset from Wieczorek 2024 model (lmax = 3000) obtained with pyshtools

Tectonic Faults

Faults are the expression of past subsurface compressional or tensile stresses that exceeded the yield strength of the crust and their distribution can be used to provide clues on the geodynamic history of a region. In this study, we used the extensively mapped fault data catalogues (Knapmeyer et al., 2006) (Figure 1), in which polylines associated with thrust (compression, N = 5,143) and normal faults (extension, N=9,675) are provided. The dataset was constructed using early Global topographic MOLA maps, which implies that the highest resolution cap for fault mapping is 4 km. While more detailed tectonic maps could be obtained using higher resolution Digital Elevation Models (DEM), such as constructed using HiRise data, the tectonic catalogue constructed by Knapmeyer et al. (2006) has sufficient resolution in the context of our work on the regional geodynamics of Noctis Mons. Using the Knapmeyer et al., (2006) catalogue, we observe a large concentration of tensile stresses around main topographies surrounding Noctis Mons (Figure 1). Tensile stresses are oriented mainly circumferential to Tharsis, along the length of Valles marineris, and the entire eastern margin of Thamusia plateau. Surrounding Noctis Mons area, although there is a large number of cross-cutting tectonics, the majority orientation is consistent with the circumferential and radial tectonic landforms the Tharsis rise likely generated (Andrews-Hanna, 2012; Sharp, 1973). This follows the marginal tensile faults around Valles Marineris coinciding with Tharsis radial faults as observed in Figure 1.

In the scope of our work, the fault orientation thus constituted a crucial aspect in explaining the tectonic nature of Noctis Mons opening (Figure 2). As discussed previously, plume upwelling beneath Noctis Mons likely began with the late Noachian–early Hesperian opening of Valles Marineris, driven by Tharsis bulge flexure (Andrews-Hanna, 2012). Thus, we observe that circumferential faults around Noctis Mons are consistent with both, tensile stress generated by a plume-related uplift beneath Noctis, and Tharsis related regional stresses (Figure 1) (Andrews-Hanna, 2012).

Geodetic Operations

In this project, we did not rely on Geographic Information System (GIS) software to map, extract and process orbital data. Rather, all operations were performed numerically using geodetic formulas on grid matrices representing elevation data and other datasets. Relevant formulas that were used include the geodetic distance, surface area and volume on a sphere. The geodetic distance d_{ij} between two grid-cell centers (φ_i, λ_i) and (φ_j, λ_j) is given by the spherical-law-of-cosines:

Equation 1

$$d_{ij} = R_{Mars}\, arccos[sin\, \varphi_i\, sin\, \varphi_j + cos\, \varphi_i cos\, \varphi_j cos(\lambda_j - \lambda_i)]$$

For a grid of shape (n × 2n) spanning the entire sphere, the uniform angular step in both latitude ($\Delta\varphi$) and longitude ($\Delta\lambda$) is given by:

Equation 2

$$\Delta\varphi\ =\ \Delta\lambda\ = \frac{360}{2n \times \frac{\pi}{180}}$$

Now, at each grid cell centered at latitude φ, the surface area A(φ) on a sphere of radius $R_{Mars} = 3389$ km is determined by:

Equation 3

$$A(\varphi) = R^2{}_{Mars}\, .\, sin(\varphi + 90^{\circ})\, .\, \Delta\lambda\, .\, \Delta\varphi$$

This gives out an area grid where for each cell on the desired grid extent we know the value of the area in km^2. Now multiplying this grid with a height component and summing over all relevant cells gives us the total volume captured by the topography.

Plume Modelling:

Because the natural convection pattern in a spherical shell forms cylindrical, plume-like upwellings, it is natural to assume that mantle plumes exist on other terrestrial planets (Schubert, Turcotte, & Olson, 2001). For Tharsis-like volcanoes, both single and multiple deep mantle plumes have been proposed as the source of heat and uplift (Schubert et al., 2001; (Kiefer, 2003). However, to create Tharsis like topography, some studies point to purely crustal processes such as isostatic uplift with flexural loading where a buoyant root pushes the surface up and bends the surrounding lithosphere (Banerdt, Phillips, Sleep, & Saunders, 1982). Phillips et al. (2001) used gravity data from Mars Global Surveyor (MGS) to determine the effect of the mass load of Tharsis on negative gravity anomalies. Their geodynamic model considered Mars' lithosphere as an elastic thin shell that when bent under Tharsis load produces the lithospheric bulge on a large scale consistent with global gravity anomalies (Phillips, 2001). According to (Redmond & King, 2004) although a thick, strong lithosphere can support volcanoes up to 24 km tall, Mars's gravity field still shows broad anomalies that simple lithospheric support can't fully explain, and are rather more consistent with moderate regional plume and/or mantle support. In this report, we investigate the topographic signal of Noctis Mons linked to a mantle plume related uplift, analogous to Tharsis Montes. Therefore the above mentioned plume models underpin two crucial aspects based on which we create a Noctis plume model in this section: (1) deep mantle plumes are a viable mechanism for generating large-scale topography on Mars' lithosphere (Schubert et al. 2001; Kiefer 2003; Redmond & King 2004), and (2) elastic flexural lithosphere models can reproduce many of the topographic anomalies consistently (Banerdt et al. 1982, 1992; Phillips et al. 2001) and can be coupled with mantle convection models to reproduce plume generated topographic uplifts through elastic flexural thin shell lithosphere.

We model a Tharsis-like plume beneath Noctis Mons using the Displacement_strain_planet (DSP) (Broquet, 2024) thin shell loading model, and estimate plume-induced uplift. Both observed elevation data and tectonic features (Knapmeyer et al 2006) are compared to the predictions from our plume model. Rather than inverting observed data, we here forward model the uplift and stress pattern associated with an input plume geometry and compare the model predictions to observations. One of the main assumptions we make here is that the dynamic plume load is compensated by flexural uplift only, which implies no crustal thickness variations. Input parameters include, the average thickness of the Martian crust, the density of the crust and mantle, as well as the elastic thickness of the lithosphere. The plume location and geometry (depth, extent, thickness) are also varied

The DSP model works in Spherical Harmonic (SH) and self consistently solves for eight different parameters including, among others, the topography (H_{lm}), lithospheric flexure (w_{lm}), Moho-depth geoid ($Gc_{,lm}$), net load on the lithosphere (q_{lm}), and tangential load potential (Ω_{lm}). A total of eight such outputs are linked to a set of five core equations for q_{lm}, w_{lm}, geoid (G_{lm}),Gc_{lm}, Ω_{lm} (Banerdt, 1986) and if any three parameters such as topography (H_{lm}), geoid (G_{lm}), crustal root variations (δclm) are pre-determined, the built in function can solve for all five equations.

Mathematically, the net load q_{lm} and lithospheric flexure w_{lm} in terms of a flexural equilibrium equation in spherical harmonics is related as (Broquet & Andrews-Hanna, 2023):

Equation 4

$$q_{lm} = g_0\,\rho_c\,(H_{lm} - G_{lm}) + g_m\,\Delta\rho\,(w_{lm} - \delta c_{lm} - Gc_{lm}) + g_M\,\delta\rho_{lm}M$$

where $\Delta\rho = \rho_m - \rho_c$ is the density contrast at the crust–mantle interface; g_0 , g_m and g_M are the vertical gravitational acceleration at the surface, crust–mantle boundary and base of the mantle density variation; and M is the thickness of the mantle density anomaly. In our work, we consider an elastic lithosphere under a classic 'Vening Meinesz' or flexural isostasy model (Philips et al., 2001; Watts, A. B. 2001). In this model, a thin elastic shell produces a regional, flexural uplift in response to a dynamic (plume only) load. The shell response is controlled by its rigidity D related as: (Tesauro et al, 2012)

Equation 5

$$D = \frac{E \times Te^{3}}{12 \times (1-\sigma^{2})}$$

where elastic modulus E and Poisson's ratio σ are given constant values, and T_e the elastic thickness of the lithosphere is used to scale the rigidity.

MARSIS Radar:

In order to conduct compositional analysis of the pyroclastic material forming the bulk of the fractured Noctis topography, we used radar data collected by the Mars Advanced Radar for Subsurface and Ionospheric Sounding (MARSIS). The MARSIS instrument aboard ESA's Mars Express has operated since 2003, and is a dual-channel low-frequency (~1 MHz) radar sounder operating from roughly 250 to 900 km altitude, using a 40 m tip-to-tip dipole antenna oriented nadir (Orosei, 2015), providing a vertical resolution about 150 m. For this instrument, synthetic-aperture processing over ~1 second of along-track acquisition yields an effective footprint of about 5 km along track and about 10 km across track. This configuration balances deep penetration, spatial resolution, and surface-clutter suppression, enabling MARSIS to map subsurface layering. By studying the mapped subsurface echoes, MARSIS can find buried layers—like ice or sediment—down to a few kilometers below the surface.

A second subsurface sounding radar, Mars SHAllow RADar sounder (SHARAD) onboard Mars Reconnaissance Orbiter has also been sounding Mars since 2006. The SHARAD instrument operates at a higher frequency (~20 MHz) than MARSIS, allowing a finer mapping of the subsurface. However, the higher frequency of SHARAD lowers the instrument's penetration depth making it inadequate to study the subsurface composition of Noctis Mons.

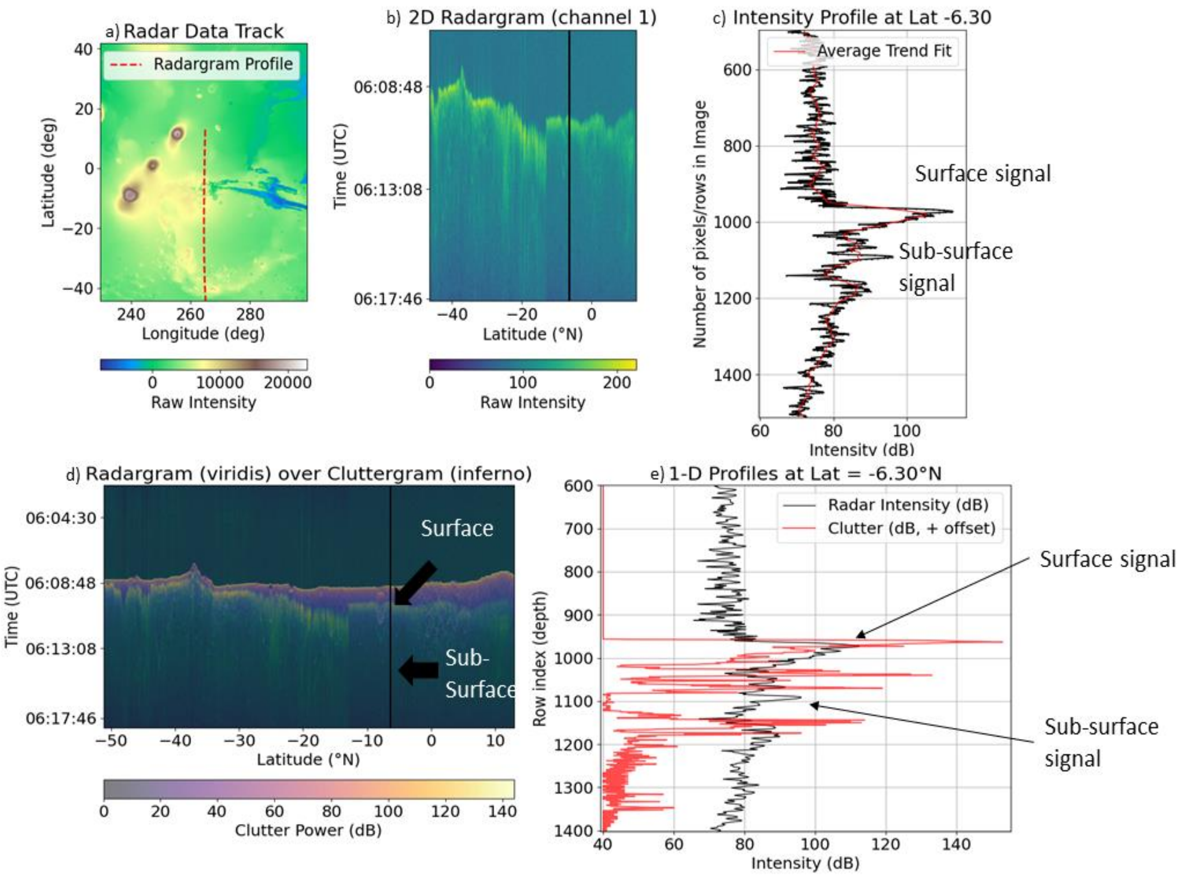

Figure 4; a) MARSIS radar track passing through Noctis Mons b) 2D radargram and selected column based on latitude c)1D intensity profile obtained for column in subplot b d) radargram comparison with clutter e) intensity profiles of radar and clutter signal at the at the same latitude

Cluttergram:

In order to determine the composition of the surface, one needs to identify radargram echoes associated with the surface and subsurface. The electromagnetic radar wave travel time within that medium can then be used to infer the dielectric properties and the composition and nature of the traversed materials. MARSIS's antenna has very low directivity, which means its radar pulse shines over the entire area under the spacecraft, not just the part directly below (the near-nadir region) where we expect to see echoes from below the surface. If the ground is rough, some of the radar pulse bounces in off-nadir directions reflecting scattered energy back to the radar. These off-nadir surface echoes arrive after the echo from the nadir point and can hide, or be mistaken for, real subsurface echoes. We call this unwanted surface backscattering from off-nadir directions "clutter." In a radargram, clutter can look like subsurface structures even though they are really just off-nadir surface echoes. To avoid such issues, we compared all our mapped subsurface interfaces against numerical electromagnetic models of surface scattering called cluttergrams. These models generate simulated surface echoes that can be compared to the actual echoes recorded by the radar (see Figure 4). If the sub-surface intensity signal shows up in both radargram and cluttergram, it can be discarded as a true indication of subsurface.

Radargram Mapping

In our workflow, we select a specific MARSIS radar track, shown by the red profile (Figure 4a), that best passes through our region of interest . From the MARSIS data product, we utilise MARSIS radargram files (the uncorrected binary ".img" and its accompanying "_geom.tab" and ".xml" metadata) by extracting calibration parameters (scaling factor and offset), data type, and the 3 image dimensions (channels, lines, samples). The raw binary is then reshaped into its multi-channel 3D form and a relevant channel is selected to produce a 2D radargram for surface-subsurface echo analysis (Figure 4).

The 2D radargram (Figure 4b) can be plotted against latitudes such that each column in the radargram corresponds with a latitude value on the map. A specific column of intensity is converted from raw counts into intensity units (decibels) using the XML-derived scaling and offset, producing a one-dimensional intensity signal profile (Figure 4c). The column is selected based on a latitude value for which the dataset passes through a thick pyroclastic deposit from the elevation grid map (Figure 11). Each major peak of the signal profile is linked to a signal from the surface and subsurface, dying down in intensity as the radar pulse penetrates deeper (Figure 4c). An overlay of the cluttergram intensity profile reveals that the signal corresponding to subsurface is clutter-free and can be considered as a subsurface signal (Figure 4e). The y axis of the intensity profile is the same set of values that make up the y axis of the radargram and therefore represent the number of pixels stacked up to make the radargram image. This means that an observed difference between the highest and the second highest intensity peaks will give us the pixel depth (Δp in equation 6) between these two signals which in essence will be the pixel depth between the surface and the signal-detected subsurface.

Dielectric Constant:

In order to estimate the dielectric constant, we obtain the apparent thickness measured by radar signal ($H_{apparent}$) and see if it is comparable to the true thickness (H_{true}) at that latitude. The true thickness is independently obtained using MOLA data. For $H_{apparent}$, we measure the pixel depth between the highest and second highest intensity signal. Since each dataset has been captured at a certain seconds/pixel resolution, obtained from the xml metadata file, we first calculate the two-way travel time for the radar signal between first impact and final reception at the instrument given by:

Equation 6

$$t_{2-way} = \Delta p \times \delta t$$

where, Δp is the pixel depth measured and δt is the seconds/pixel resolution constant and equals 0.35714×10^{-6} seconds/pixel for the dataset used here. Following this, the apparent thickness ($H_{apparent}$) of a medium through which electro-magnetic waves penetrate and emit after reflection (hence $t_{2\text{-way}}$) can be related by:

Equation 7

$$H_{apparent} = \frac{(c \times t_{2-way})}{2}$$

If the $H_{apparent}$ values are comparable to H_{true}, we proceed with the formula for permittivity (or dielectric constant) for a medium of a true thickness (H_{true}) in which electro-magnetic waves propagate given by:

Equation 8

$$\varepsilon_{\ medium} \simeq \left(\frac{c \times t_{2-way}}{2 \times H_{true}}\right)^2$$

Now, from Figure 4 (b), each column may correspond to different values of pixel depth depending on the latitude and the thickness H_{true} at which the column sample is extracted. We will use a mean of three such columns of three different ε values to get an estimate of the mean dielectric constant of the material beneath the Noctis Mons.

Results and Discussion:

Reconstructing the Noctis Mons

The current topography of Noctis Mons is heavily fractured. This section deals with construction of topographic elevations of pre-fracture Noctis Mons. In order to achieve this, we work with interpolation of present day MOLA topography data. Observations reveal (Figure 3) that the current topography of Noctis Mons is fractured such that some parts remained elevated like flat mesas (Lee & Shubham, 2024) after inward gravitational caldera collapse (Figure 2d). Around these elevated flat mesas (hereafter raised surface), the low depressions (hereafter base surface) expose the anticipated base of the Noctis Mons on top of which pyroclastic deposits once accumulated to form the Noctis edifice. Therefore, one can interpolate both the raised surface and base surface by first sampling elevation data points from each surface and then interpolating the sampled elevation values over the entire extent of the Noctis Mons region. Interpolating the raised surface within Noctis reconstructs a pre-fractured Noctis shape (Figure 5). Similarly, interpolating the sampled elevations from the exposed base surface reconstructs the continuous pre-collapse basement topography across the Noctis Mons region (Figure 5).

Since Noctis Mons is a pile of pyroclastic and basaltic deposit (Lee & Shubham, 2024) on top of a plume-uplifted plain (Figure 2c), we can also interpolate far from Noctis i.e., removing the region of current volcanic deposits (Figure 7a) and interpolating to get the regional plume-induced uplifted plain (Figure 7b). We call this grid 'pre-Noctis uplifted plain', implying the plume-related uplift before Noctis pyroclasts were deposited. In this way, a summation of the pre-Noctis uplifted plain and the interpolated raised surface yields the full volcanic construct of Noctis Mons before fracturing (Figure 6b), comparable to other Martian volcanoes (Figure 6d). Finally, by subtracting our interpolated base surface from the current elevation (Figure 3), we obtain the present-day thickness of the Noctis Mons pyroclastic deposits (Figure 11a). This "thickness grid" (H_{true}) is what we compare to the apparent thickness ($H_{apparent}$) in Equation 7, and then substitute into Equation 8 to estimate the dielectric constant (ε_{medium}) beneath the volcanic layer.

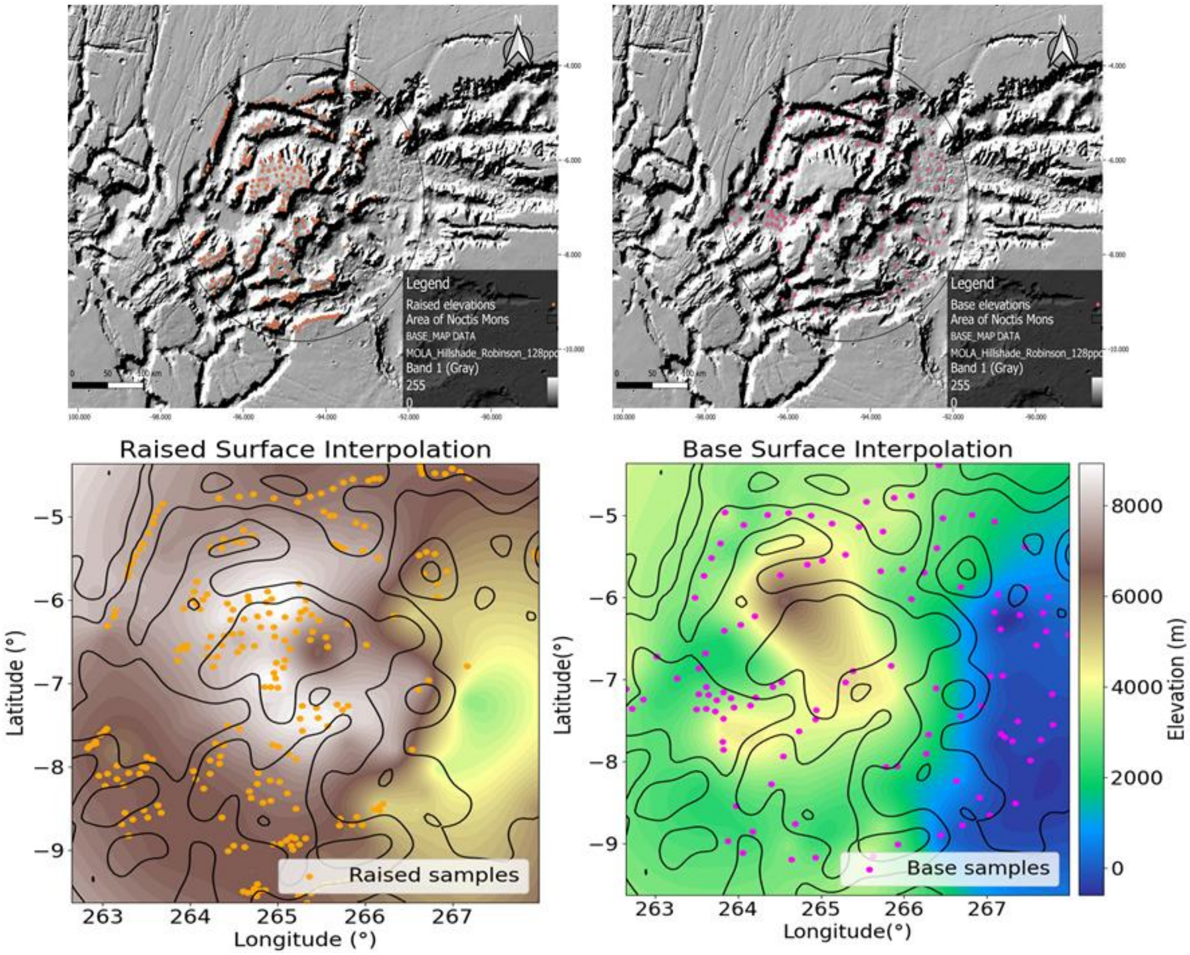

Figure 5: Top row of subplots show Global MOLA Hillshade basemap rasters of the Noctis Mons area with raised and base elevations (scale of these images is 0-100 km). The raised and base topography is sampled with data points (orange and violet) in the QGIS environment as shown. The bottom row of plots shows interpolated grids generated from each sampled dataset.

The mean profile over reconstructed Noctis Mons (Figure 6c) is distinct from the mean profile over present day fractured topography (Figure 8b). This is significant because while the fractured plains are not entirely removed in the reconstructed Noctis shape, a conical

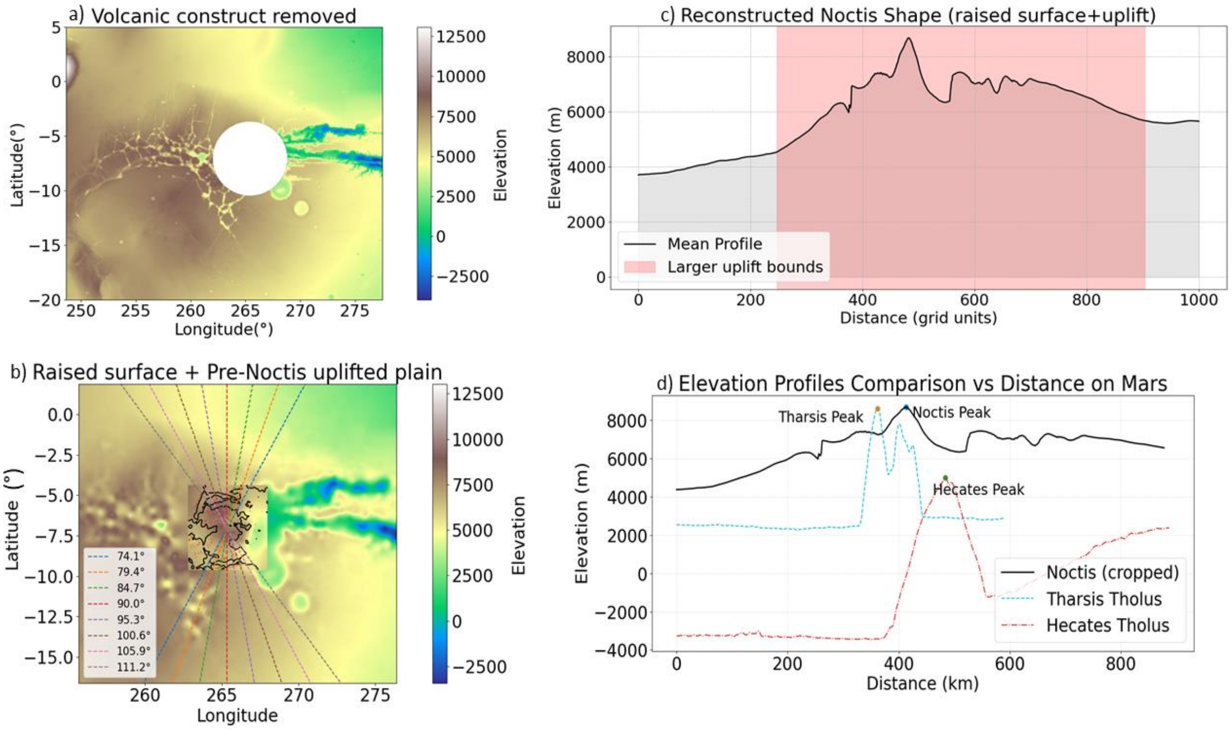

Figure 6: a) Noctis volcanic construct is masked to interpolate for regional uplift; b) interpolated raised surface is added on top of the regional pre-Noctis uplift (see Figure 7b) gives a reconstructed Noctis Mons and c) a mean of elevation profiles is plotted over this reconstructed shape; d) comparison of reconstructed Noctis Mons elevation with relative scale volcanoes (lower right)

topography missing in the present day Noctis elevation profile (Figure 8b) is certainly retrieved, with a distinct peak reaching up to an elevation of 8693.61 meters. This peak (~8694 m) aligns with the 8000–9028 m fractured-block elevations reported by Lee et al. (2024) for the 250 km wide Noctis volcanic region. By comparison, Tharsis Tholus (13.4°N, 269.3°E), an intermediate-sized shield volcano located in the eastern Tharsis, spans ~150 km and rises ~ 8-9 km (higher on western flank), exhibiting steep, fault-bounded flanks and a central caldera-collapse feature, possibly mirroring the plume-supported uplift and dyke-fed flood basalts we infer for Noctis Mons (Platz, 2011). Another similar-sized dome-shaped volcano called Hecates Tholus (32.1° N, 150.2° E), in contrast, is a wider (∼182 km), ~5 km-high shield with nested calderas and evidence of both effusive and late-stage explosive activity (Fassett, 2006). See Figure 6d for a comparison of elevation profiles.

We derived a pre-fracture thickness grid by subtracting the uplifted plateau from the raised surface (Figure 7d), then restricted it to elevations ≤ 1.5 km and longitudes ≥ 267° to isolate pyroclastic deposits. This thickness data can be used with the area grid we developed (equation 3) previously. This operation yields a total uplifted Noctis volcanic volume of 0.75×10^6 km^3.

For comparison, this sits between Pavonis Mons (~ 0.25 × 10^6 km^3) and Ascraeus Mons (~ 1.2 × 10^6 km^3), highlighting Noctis Mons as a major Tharsis volcanic edifice.

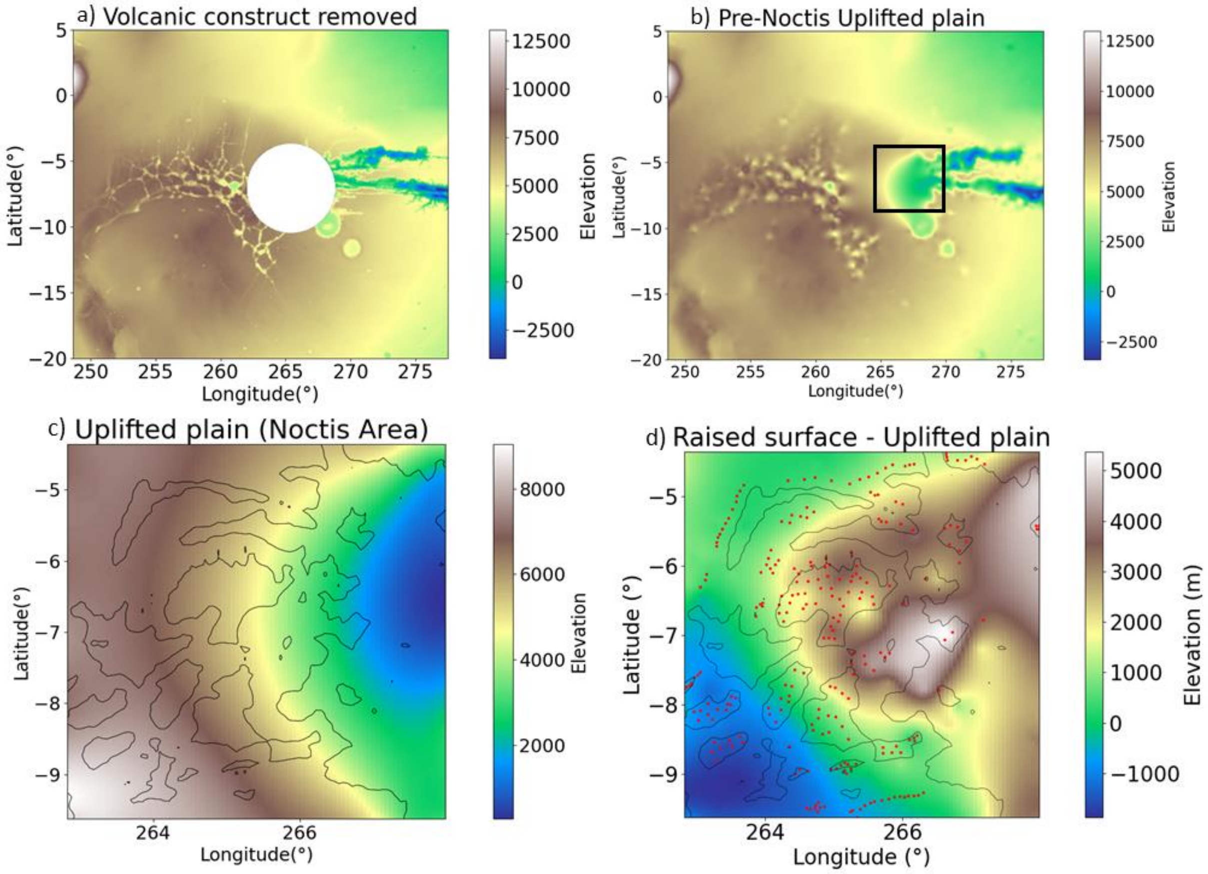

Figure 7: a) Present-day Noctis volcanic construct Masked; b) Interpolation of the surrounding area to model regional plain uplift; c) The uplifted Noctis-area plain (from 7b); d) Removing uplift from (pre-fracture) raised surface reveals the pre-Noctis volcanic construct whose volume we can estimate.

The Topographic Uplift

The next in line of investigation is the estimation of the topographic uplift affected by a hypothesised plume underneath Noctis Mons. As depicted in the schematic figure (Figure 2b), a plume head creates a flexural uplift. It is on top of this uplift that pyroclastic materials of the shield volcano are deposited in later stages (Figure 2c). There are two possible ways to obtain the topographic uplift in two dimensional space. One is to mark the point of inflection or observed change in the topographic elevation profile with respect to the regional slope. If we take a mean of elevation profiles over current Noctis topography (Figure 8b), it is possible to visibly locate points of inflection in elevation profiles where a significant change in steepness of the profile towards Noctis, compared to the regional slope, can be assumed to indicate plume-induced uplift (see red shade in Figure 8b). The second method involves marking tectonic faults as proxies for the boundary of the uplifted region. We employed both methods of marking uplift and found no perceptible difference between their results. For our discussion, we will consider the uplift obtained by tectonic features as markers of plume generated uplift, for simplification. From the fault distribution data (Knapmeyer et al, 2006) we select two circum-Noctis tectonic faults (marked by cross in Figure 8a) close to Noctis and sample an elevation profile over them. The part between the two opposite circum-Noctis faults is shaded with yellow in the mean elevation profile (Figure 8c). This gives us the range of noise in elevation profile that can be masked and interpolated over. We fit a spline function of smoothing parameter, $s = 10^7$, as Figure 8c depicts and obtain a close proxy for an "observed uplift" elevation profile. This "observed profile" is detrended for simplification (Figure 8d), and is used for comparison with numerically modeled uplift in the next section.

Modeled Plume Uplift:

In this section we compare the obtained observed profile of uplift with a plume-generated numerical model of uplift (hereafter "plume-uplift"). We model this plume using the DSP tool described previously. For a dynamic uplift, the system does not change/adjust its crustal root thickness to compensate for topographic load. This means, surface displacement (uplift) can be entirely attributed to the plume's effect. Because there's no contribution from variations in load crustal thickness, any change in the dynamic uplift (w_{lm}) will come directly from the parameters governing the mantle plume (see equation 4). This means, we can define a circular anomaly for a plume on a grid with a controllable set of parameters such as plume radius (PR), density anomaly (DA), and longitudes and latitudes of the center of the circular plume. The DSP system allows further modifications such as plume thickness (assumed vertical length of the plume) and elastic thickness (Te) of the lithosphere.

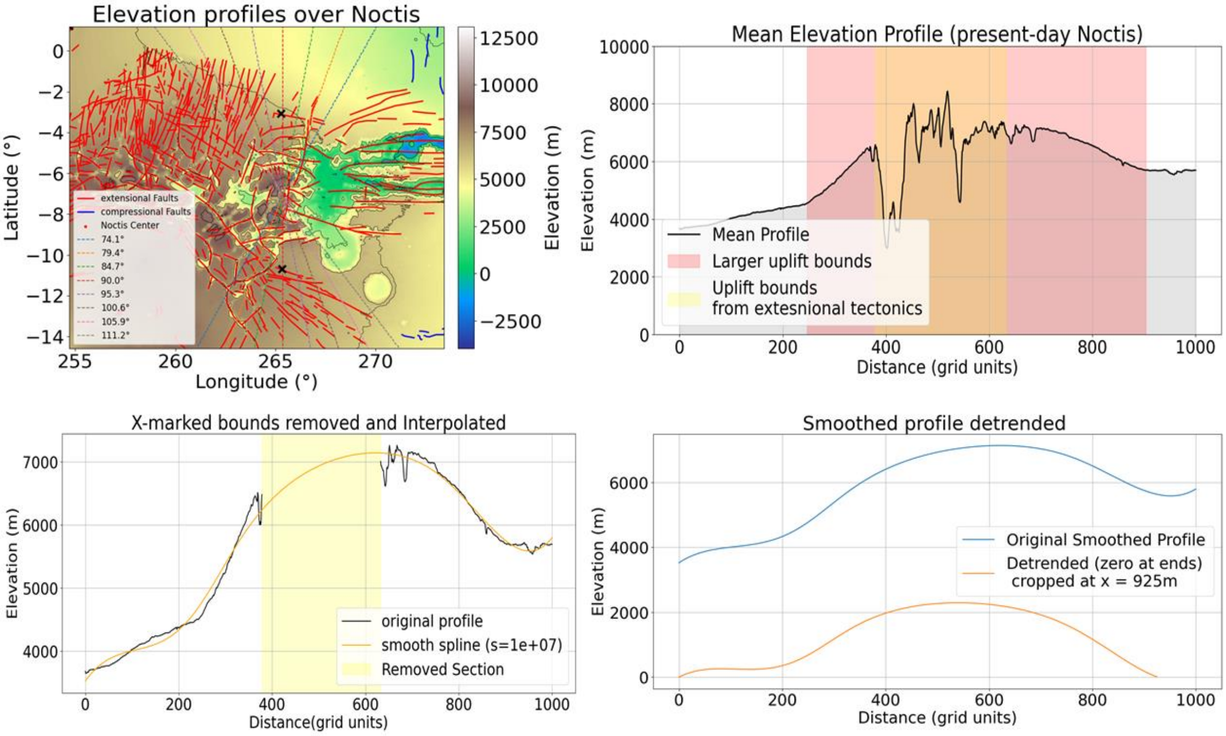

Figure 8: Two opposite tectonic markers identified on MOLA map (Knapmeyer et al., 2008) (top left); Marked uplift bounds between tectonic markers in mean elevation profile (top right); Uplift bounds are masked and fitted over with a smooth spline (lower left); Smoothed profile is detrended and cropped at one end to avoid negative elevation values (lower right).

We define this circular anomaly on a separate grid using a Gaussian profile for smooth edges and integrate it into the DSP tool (Figure 10a). This gave us a plume whose flexural uplift (w_{lm}) can be modified by editing the associated set of parameters governing this uplift in the system. In order to estimate best fit parameters, we iterate over a range of values for the Elastic

Thickness (Te) in km, Density Anomaly of the plume with respect to the mantle (DA) in kg/m^3, Plume radius (PR) in km, center latitude, and center longitude (degrees). Eventually, we obtain a 5D matrix for all the different combinations produced and by collapsing 3 axes at a time we can analyse a set of 2 parameters on a 2D mesh grid representing the smallest RMS (root mean square) misfit given by:

Equation 9

$$RMS = \sqrt{}(\frac{1}{N}\sum_{i=1}^{N} = 1\ (p_i^{plume} - p_i^{Noctis}))^2$$

where p_i is the uplift profile from the plume model and uplift profile observed respectively. In other words, the best fit values for each individual parameter that was modified through each iteration can be obtained from 2D RMS misfit plots (Figure 9). The iterations gave out an overall minimum RMS misfit value of 127.35 meters i.e., lowest value over the entire 5D matrix. The parameter values at this misfit obtained are as follows: Density Anomaly (DA) of -105 kg/m^3—which is the measure of buoyancy for plume rise such that a more negative density contrast creates more buoyancy and warmer plume, resulting in greater uplift at the surface. The Plume Radius (PR) at the minimum misfit is 473.3 km, the Elastic Thickness (Te)

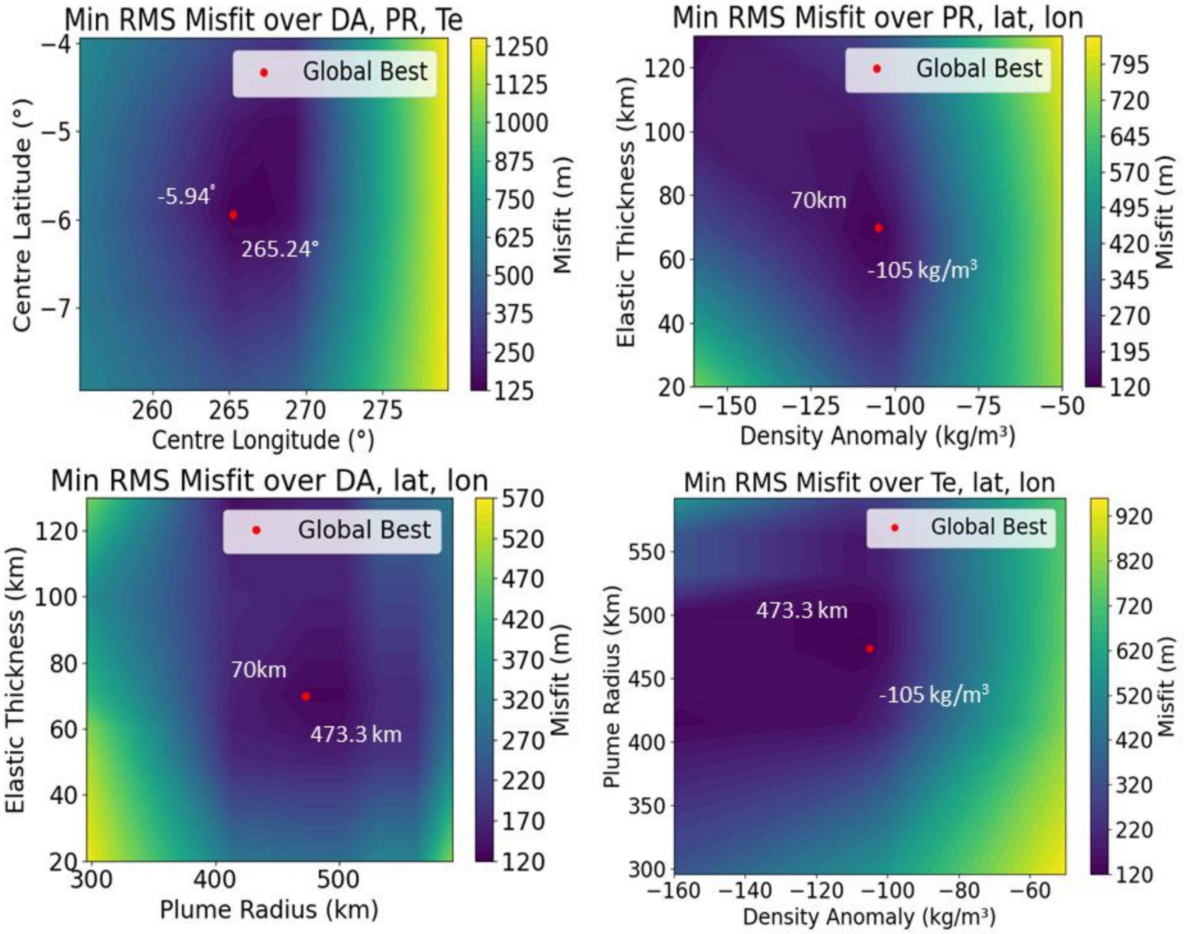

Figure 9: The 5D misfit array is collapsed over three axes at a time and the remaining two axes are plotted in different combinations with global best fit results pointed red in the mesh grids

at this misfit measured 70 km while the latitude and longitudes of the plume center were best fitted at -5.94° and 265.24° respectively.

Although the range of values over which these iterations were made were selected such that a larger perceivable misfit is easily recognized, one can incorporate a measure of standard deviation to provide uncertainties over the misfit values obtained. By computing the mean elevation profile's (Figure 8b) standard deviation at each sample point and constructing two profile offsets by $+1\ \sigma$ and $-1\ \sigma$, one can generate upper and lower boundary splines within the range of plausible Noctis elevations. These boundary splines can then be compared directly against our obtained best-fit model: for each boundary case, we could evaluate the misfit between the observed ($\pm 1\ \sigma$) spline and the modeled profile. Although we have not implemented this procedure here, it offers a straightforward means to incorporate observational uncertainty in a future work. Once these parameter values are obtained, we plug them into the DSP code with a circular plume anomaly whose best parameters we just obtained. This gives a best fit plot of the plume generated uplift compared against the observed uplift. (Figure 10b).

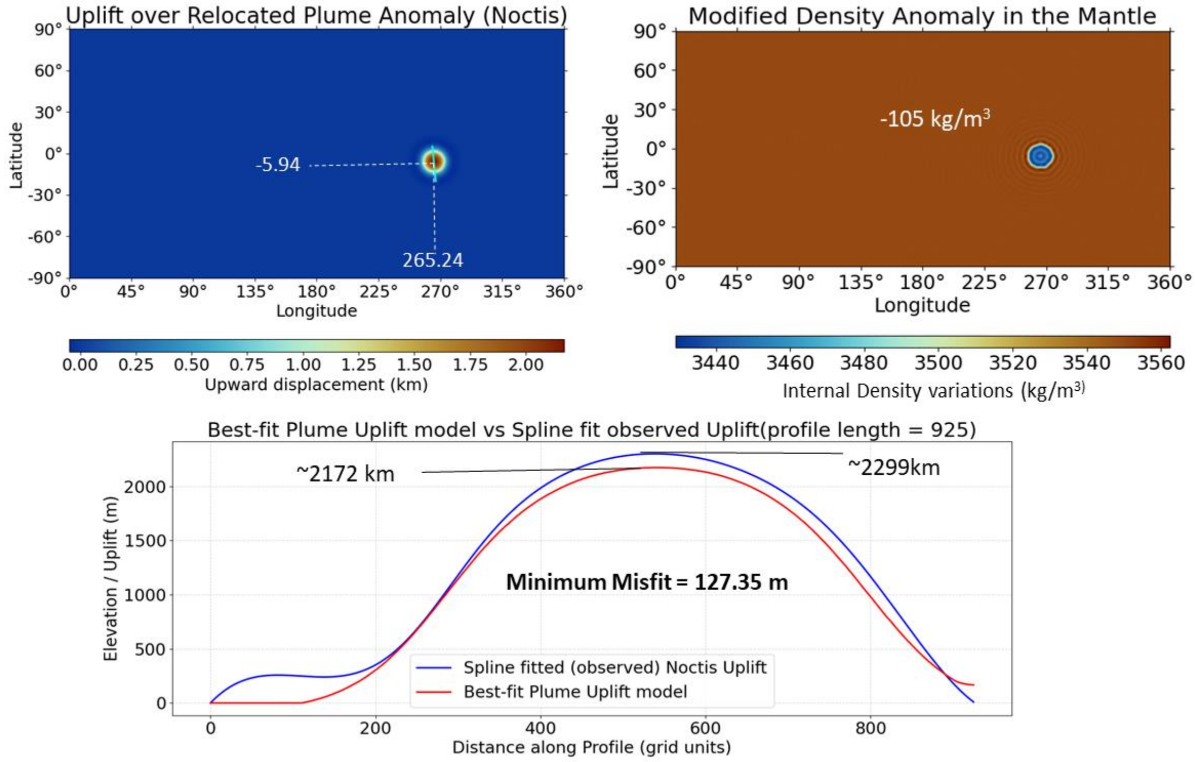

Figure 10: a) elevation profile over circular plume-related uplift (top) b) best-fit plume uplift model vs observation (bottom)

Compositional Analysis: MARSIS

As discussed previously, the dielectric permittivity difference recorded by the Radargram can be used to estimate the composition of the subsurface involved. The low-frequency permittivity of a three-phase mixture (basalt, ice, and air) can be approximated by a power-law mixing formula (Stillman, 2010):

Equation 10

$$(\epsilon_{mix})^{1/\gamma} = \Phi_{basalt}(\epsilon_{basalt})^{1/\gamma} + \Phi_{ice}(\epsilon_{ice})^{1/\gamma}$$

where, ϵ_{mix} is the dielectric constant of the mixture under examination; ϵ_{ice} is the permittivity of pure ice, taken here as 3; ϵ_{basalt} is the dielectric constant for basalt which we take as 9.8 based on SHARAD measurements in the Tharsis region (Carter, 2009) γ is an empirical exponent that captures how the phases are geometrically distributed such as grain contacts and pore shapes. In sand-ice-air mixtures, values of γ near 2.7 often best reproduce laboratory measurements (Stillman et al., 2010), reflecting the

loosely packed, granular nature of rock, ice, and void. The equation 10 therefore provided a straightforward way to invert the measured static permittivity ϵ_{mix} to estimate how much ice (or air) is present in a basaltic matrix. In order to estimate the static permittivity ϵ_{mix}, we required the true thickness of the pyroclastic material forming bulk of Noctis. As described in previous sections, this is obtained by subtracting interpolated base surface from current Noctis topography. We used the thickness grid thus obtained to extract three latitudinal points for three values of ϵ_{mix} and obtain three 1D intensity profiles (Figure 11) for pixel depth Δp (equation 6) calculation. The mean of three randomly chosen ϵ values comes out to be ~3.90 as denoted by ϵ_{mix} and plugged into equation 10. We also measured a standard deviation of 2.29 from the mean value represented by error bars in Figure 12.

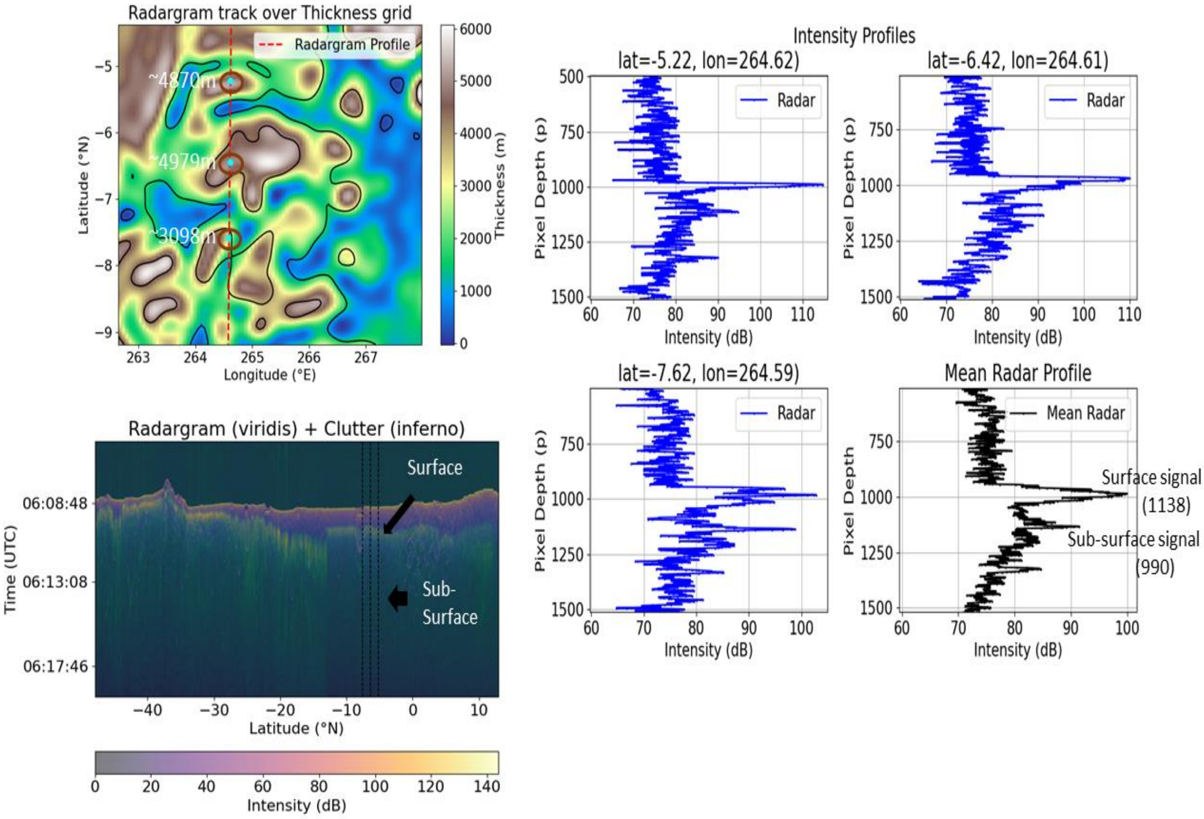

Figure 11: Radargram extracted at indicated latitudinal positions with associated thickness values (top left). Radargram and clutter where the profiles are extracted (bottom left). 1D profiles of intensity signals at the three indicated points (right) and their mean value which is used to calculate ϵ_{mix} (equation 8)

From equation 10, we explore two possible scenarios. Either the mixture has ice content as some studies suggest (Lee et al 2023) or the spaces are filled with voids that make a porous pyroclastic mixture. Assuming a two phase mixture model of basalt and ice (with no pores), their volume fractions must sum to unity ($\varphi_{basalt} + \varphi_{ice} = 1$). Similarly, if the only other component is void spaces, the volume fraction will be $\varphi_{basalt} + \varphi_{air} = 1$. Since we know ϵ_{mix}, we can rearrange equation 10 to solve directly for how much basalt is in the mixture. It can be established that two possibilities exist as far as the bulk composition of Noctis Mons is concerned: a) a mixture of 19% basaltic and 81% ice component and b) a basaltic rock of 51% porosity implying porous pyroclastic deposits.

Numerous studies have argued in the past for present-day subsurface ice on Mars. Ground ice played a crucial role in early volcanic geomorphology of Mars as theoretical models such as by Wilson and Head (2007) explain. Lee et al., (2024) proposed an ice substrate beneath present-day Noctis Mons, covered by a layer of ~1-3 m thick pyroclastic deposits. Following this, while a few meters thick ice substrate can indeed be suspected, a value of 81% volume fraction for a thickness between 4-5 km is disproportionately large, and would be clearly visible, as a bright, featureless unit analogous to the North Polar cap, in MARSIS radar-grams, which was not observed. The second possibility involves a porous pyroclastic deposit which, as many studies have reported, is likely a result of dykes feeding effusive style flood basalt magma (Head et al., 2006; Wilson and Head, 1994) in combination with eruptive phreatomagmatism depositing porous pyroclastic ash (Figure 2) (Wilson and Head, 2007).

However, it can be considered that a small fraction of ice is likely a part of this porous basalt, i.e., ice component contributing some fraction in the porous basalt. Our results show that an ice substrate beneath Noctis Mons is a likely possibility, especially when coupled with the CRISM analysis results of Lee et al., 2024 where ~1-3 m thick pyroclastic deposits are reported in the Noctis regions as protective covers over ice substrate. Furthermore, Lee et al., 2023 have also argued in favour of a relict glacier feature at the site of Noctis Mons after identifying glacial signatures such as crevasses and moraines which is indicative of a) remnant ground-ice as well as b) past ice-magma interaction features called "blistered terrains' of rootless cones. From here we suggest that both effusive style basaltic lava flows and explosive phreatomagmatic pyroclastic ash flows once existed in Noctis Mons.

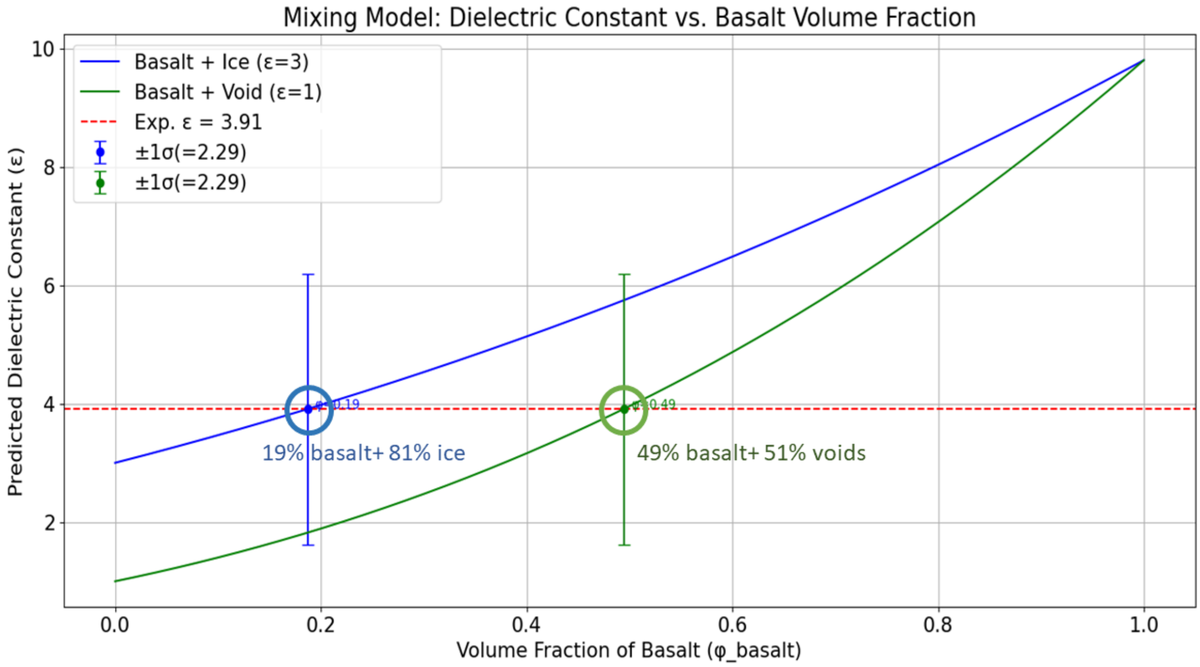

Figure 12: Mean epsilon of the volcanic deposits indicates a basaltic porous mixture and/or basalt lying over ice substrate can be expected.

Conclusion:

In conclusion, a number of geophysical and geodynamic investigations were conducted to build a pre-deformation Noctis elevation, volume, and topographic uplift, and to assess a plume-generated uplift scenario along with the characterization of subsurface composition. Our findings suggest that the currently fractured Noctis Mons was once, likely, a plume-supported medium to low-sized shield volcanic edifice. Dynamic uplift beneath the Noctis lithospheric load was supported by a 70 km thick plume head sitting at the base of a 70 km thick lithosphere and expanding across ~ 470 km, within the larger uplift of Noctis Mons. The composition of the volcanic construct, hints towards a likelihood of a predominant distribution of porous basaltic and pyroclastic ash deposits that occur in a combination with a fraction of subsurface ice presently, that influenced its geomorphology previously, in the Noctis Mons region. Furthermore, a magma-water interaction resulting in formation of "rootless cones" through phreatomagmatism also occurred here, as revealed by our compositional analysis in consistency with observations made through orbital data. This volcanic construct lies on top of an uplifted plain whose uplift mechanism is estimated using an analytical elastic flexure model for thin lithospheric shell where the plume-head generated load directly translates to the topographic signal on top of which Noctis volcanic construct lies.

Although previous studies used CRISM analysis and other orbital-datasets for chemical and mineralogical characterization in the Noctis Mons region, we present the first geophysical and geodynamic work that better constrains the geomorphological history of Noctis Mons. Unlike previous studies, this work numerically determines a set of plume related parameters that help us better understand the geodynamics beneath Noctis Mons in relation to its shared chronological and geological history with major Martian topographies such as Tharsis Montes and Valles Mariners. Similarly, complimenting previous works, our inferences derived using MARSIS radar grams and dielectric permittivities limit the compositional analysis of volcanic subsurfaces of Noctis Mons as they lie consistent with previous observations about pyroclastic deposits and consolidate the hypothesis on the presence of ice substrate. Finally, bridging the gaps between previous analysis of topographical datasets, our interpolation results provide a reconstructed history of the currently fractured ancient Noctis Mons shield edifice which will help understand the local and regional geomorphology of the neighboring regions.

Our plume model is adapted for a simplified scenario with zero crustal root variations that makes the comparison with a smoothed out observation less complex, especially since we are dealing with a heavily fractured topography with a large noise component in the elevation dataset. Certain limitations can also arise from the smoothing of the observed data while we prepare it for comparison with the plume model. Additionally, although we have estimated parametric values for a plume related uplift, we did not in this study set boundary conditions to define limitations for error range over these values. The compositional fraction measured for basalt and ice fractions can also be improved to define precise fractions of ice, which we did not explore in the present scenario.

Future work can integrate high-resolution crater-count chronometry with cross-cutting relationship analysis to refine Noctis's formation age; apply targeted geophysical and spectral methods to constrain the composition and stratigraphy of its subsurface ice column; and couple global stress-field models with detailed fault-orientation mapping to correlate the tectonic controls on its structural evolution. Based on the applied datasets, developed methods, and observed results, we interpret Noctis Mons as an ancient shield volcanic edifice built over a plume supported uplifted plain. The volcanic construct is a result of a combination of effusive flood basalt magmatism and eruptive phreatomagmatism in combination with groundwater and ice substrates. Our interpretations further the understanding of geomorphological history of Noctis Mons region and contributes to a part of the larger question "Is Noctis Mons really an ancient Martian volcano?"

Bibliography

Andrews-Hanna, J. (2012). The formation of Valles Marineris: 1. Tectonic architecture and the relative roles of extension and subsidence. *Journal of Geophysical Research (Planets)*.

Banerdt, W. B., Phillips, R., Sleep, N., & Saunders, R. (1982). Thick shell tectonics on one-plate planets: Applications to Mars. *J. Geophys. Res., 87(B12), 9723–9733,*.

Broquet, A. (2024). Displacement_strain_planet: 0.5.0 (Version 0.5.0). doi:http://doi.org/10.5281/zenodo.4916799

Broquet, A., & Andrews-Hanna, J. (2023). Geophysical evidence for an active mantle plume underneath Elysium Planitia on Mars. *Nature Astronomy 7*, 160–169.

Carr, M. (1987). Water on Mars. *Nature 326*, 30–35 .

Carr, M. H. (2007). *The Surface of Mars.* Menlo Park: Cambridge Planetary Science.

Carter, L. M. (2009). Radar remote sensing of pyroclastic deposits in the southern Mare Serenitatis and Mare Vaporum regions of the Moon. *J. Geophys. Res., 114, E11004,*.

Fassett, C. I. (2006). Valleys on Hecates Tholus, Mars: origin by basal melting of summit snowpack. *Planetary and Space Science, Volume 54, Issue 4,*.

H. Carr, M., & W. Head, J. (2010). Geologic history of Mars. *Earth and Planetary Science Letters*, 185-203. doi:https://doi.org/10.1016/j.epsl.2009.06.042.

Harder, ,., & Christensen, U. (1996). A one-plume model of martian mantle convection. . *Nature 380,* , 507–509 .

Harrison, K. P., & Grimm, R. E. (2008). Multiple flooding events in Martian outflow channels. *Geophys. Res., 113, E02002,*.

Hauber, E. P. (2011). Very recent and wide-spread basaltic volcanism on Mars. *Geophys. Res. Lett., 38, L10201*.

Head, J. W. (2002). Northern lowlands of Mars: Evidence for widespread volcanic flooding and tectonic deformation in the Hesperian Period. *J. Geophys. Res., 107(E1)*.

Head, J. W. (2006). Modification of the dichotomy boundary on Mars by Amazonian mid-latitude regional glaciation. *Geophys. Res. Lett., 33, L08S03*.

Ivanov, B. (2001). Mars/Moon Cratering Rate Ratio Estimates. *Space Science Reviews 96,*, 87–104. doi:https://doi.org/10.1023/A:1011941121102

Kiefer, W. S. (2003). Melting in the Martian mantle: Shergottite formation and implications for present-day mantle convection on Mars. *Meteorol. Planet. Sci., 38, 1815–1832.*

Knapmeyer, M. e. (2006). Working models for spatial distribution and level of Mars' seismicity. *J. Geophys. Res., 111*.

Lee, P., & Shubham, S. (2024). LARGE ERODED VOLCANO COMPLEX AND BURIED GLACIER ICE IN EASTERN NOCTIS LABYRINTHUS: EVIDENCE FOR RECENT VOLCANISM AND GLACIATION NEAR MARS’ EQUATOR. *55th LPSC.*

McSween, H. (2002). The rocks of Mars, from far and near. *Meteoritics & Planetary Science, 37*.

Metz, J. (2010). Thin-skinned deformation of sedimentary rocks in Valles Marineris. *J. Geophys. Res., 115, E11004*.

Montgomery, D. (2006). Continental-scale salt tectonics on Mars and the origin of Valles Marineris and associated outflow channels. *Geological Society of America Bulletin - GEOL SOC AMER BULL*.

Orosei, R. (2015). Mars Advanced Radar for Subsurface and Ionospheric Sounding (MARSIS) after nine years of operation: A summary. *Planetary and Space Science, 112*, 98-114.

Phillips, R. J. (2001). Ancient geodynamics and global-scale hydrology on Mars. *Science, 291, 2587–2591.*

Platz, T. (2011). Vertical and lateral collapse of Tharsis Tholus, Mars. *Earth and Planetary Science Letters, Volume 305, Issues 3–4,*.

Poulet, F. (2005). Phyllosilicates on Mars and implications for early Martian climate. *Nature 438.*, 623-627.

Redmond, H. L., & King, S. D. (2004). A numerical study of a mantle plume beneath the Tharsis Rise: Reconciling dynamic uplift and lithospheric support models. *J. Geophys. Res., 109, E09008*.

Schubert, G. D., Turcotte, L., & Olson, P. (2001). Mantle Convection in the Earth and Planets. *940 pp., Cambridge Univ. Press, New York.*

Smith, D. E. (2001). Mars Orbiter Laser Altimeter: Experiment summary after the first year of global mapping of Mars. *J. Geophys. Res., 106(E10), 23689–23722*.

Squyres, S. W. (2007). Pyroclastic Activity at Home Plate in Gusev Crater, Mars. *Science 316*, 738-742.

Stillman, D. E. (2010). Low-Frequency Electrical Properties of Ice-Silicate Mixtures. *J. Phys. Chem. B 2010, 114, 6065–6073*.

Tanaka, K. L. (2014). The New Geologic Map of Mars: Guiding Research and Education. *Eos Trans. AGU, 95(38)*, 341.

Thorarinsson, S. (1953). The crater groups in Iceland. *Bull Volcanol 14, 3–44 (1953)*.

Webb, B., & Head, III, J. (2002). Noachian Tectonics of Syria Planum and the Thaumasia Plateau. *Lunar and Planetary Science Conference*, 1358.

Wieczorek, M., & Meschede, M. (2018). SHTools — Tools for working with spherical harmonics. *Geochemistry, Geophysics, Geosystems, 19,* , 2574-2592,.

Wilson, L., & Head, J. (2007). Explosive volcanic eruptions on Mars: Tephra and accretionary lapilli formation, dispersal and recognition in the geologic record. *Journal of Volcanology and Geothermal Research Volume 163, Issues 1–4,*, 83-97.

Wilson, L., & Head III, J. (1994). Mars: Review and analysis of volcanic eruption theory and relationships to observed landforms. *Rev. Geophys., 32(3)*, 221–263.